

α clustering from the formation of a pocket structure in the α -nucleus potentialHailan Zheng ^{1,2}, Daming Deng ^{2,*} and Zhongzhou Ren^{1,†}¹*School of Physics Science and Engineering, Tongji University, Shanghai 200092, China*²*College of Physics and Optoelectronic Engineering, Shenzhen University, Shenzhen 518060, China*

(Received 14 August 2023; revised 10 November 2023; accepted 27 November 2023; published 3 January 2024)

We investigate the formation of a pocket structure in the α -nucleus potential based on the dynamic double-folding potential model. We improve the model with the density-dependent Migdal nucleon-nucleon (NN) interaction and combine it with the nuclear medium effect. The improved potential naturally generates a pocket structure at the nuclear surface, which physically agrees with the characteristics suggested by the microscopic many-body calculations. The result reveals that the formation of the pocket structure is due to the strong Pauli repulsion caused by the variation of the NN interaction when the α cluster and the daughter nucleus have large density overlaps. The existence of the nuclear medium effect is essential to the physical self-consistency of the pocket position. These findings highlight the importance of the medium effect on the NN interaction and provide solid theoretical support for the understanding that α clustering occurs at the surface of heavy nuclei.

DOI: [10.1103/PhysRevC.109.L011301](https://doi.org/10.1103/PhysRevC.109.L011301)

The investigation of α -cluster formation in finite nuclei has been a longstanding topic in nuclear physics [1–6]. The α -clustering phenomenon arises from the α correlation which depends on both the pairing and the neutron-proton correlations. Previous research on the competition between various nucleon correlations in homogeneous nuclear matter has revealed that the α correlation becomes prominent only when the nuclear density is below a specific value [7–9]. This critical density, identified as the Mott density associated with the formation of the α cluster, was estimated to be about 1/5 of the saturation density in many-body calculations [7,9,10].

In heavy nuclei, the α cluster tends to form at the nuclear surface because the low-density condition mentioned above is typically satisfied in this region [10–12]. As an example, the α -formation amplitude of ^{212}Po , calculated with the basis of a combined shell-and-cluster-model ansatz, shows a significant peak at the surface region, indicating the location of the formed α cluster [11]. Due to the existence of Pauli blocking, the α cluster formed in nuclei usually exhibits a larger spatial distribution. In the description of the quartetting wave function approach (QWA), the combined effect of the mean field and Pauli blocking, namely the medium effect, leads to a pocket geometry in the effective potential for the α -daughter system [10,13–15]. The resulting quartetting wave function, constrained by this pocket structure, also exhibits a peak at the nuclear surface self-consistently [14,15].

Recently, the dynamic double-folding potential (DDFP) model for α decay was proposed [16,17]. The DDFP model significantly improves the agreement between calculated and experimental half-lives by incorporating the medium effect into the double-folding α -nucleus potential. However, upon

the surface geometries of the DDFP and the potential derived from the QWA, a notable difference can be recognized: the pocket structure, as a typical feature responsible for the clustering phenomenon in nuclei, is absent in the DDFP. Considering that the pocket geometry originates from the existence of the medium effect, in this Letter, we explore the underlying mechanism inside the formation of the pocket structure based on the DDFP model.

In the DDFP model, the nuclear and the Coulomb potentials for α -daughter system are of the following formalism [16,17]:

$$V_N(\mathbf{R}) = \int \rho_1(\mathbf{r}_1)\rho_2[\mathbf{r}_2, \rho_1(\mathbf{R})]v_N(s, \rho_1, \rho_2) d\mathbf{r}_1 d\mathbf{r}_2, \quad (1)$$

$$V_C(\mathbf{R}) = \int \rho_1(\mathbf{r}_1)\rho_2[\mathbf{r}_2, \rho_1(\mathbf{R})]v_C(s) d\mathbf{r}_1 d\mathbf{r}_2. \quad (2)$$

The medium effect of the α cluster is embodied in its density distribution

$$\rho_2[\mathbf{r}_2, \rho_1(\mathbf{R})] = \rho_{2,s}(\mathbf{R}) \exp\{-\beta[\rho_1(\mathbf{R})]r_2^2\}. \quad (3)$$

The density-dependent width parameter β is described by $\beta[\rho_1(\mathbf{R})] = \frac{0.7024}{1 + \frac{45}{16\rho_{1,s}}\rho_1(\mathbf{R})}$, which satisfies the critical constrains of medium effect from the microscopic calculation [10,16,17]. The nucleon-nucleon (NN) interaction v_N adopts the density-dependent M3Y-type interaction, specifically, the CDM3Y6 interaction [18]. Since the parametrized form of the M3Y interaction is derived by reproducing the scattering data near the nuclear surface, it provides a good description of the NN interaction in low-density regions [19]. However, previous studies have pointed out that the M3Y interaction or its density-dependent form is insufficient to describe the strong repulsion in large density-overlap regions [20–22]. Realizing that the medium effect also manifests itself in the double-folding process through the density-dependence in the NN

*ddm@szu.edu.cn

†zren@tongji.edu.cn

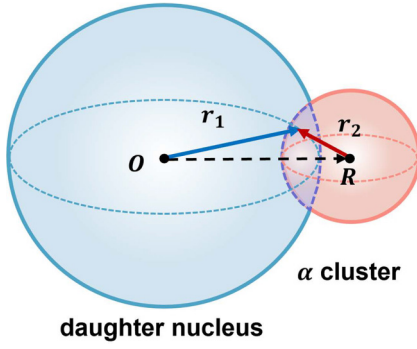


FIG. 1. Schematic of the coordinates used in the spherical double-folding potential model. The vector between the interacting nucleons, defined as $s = \mathbf{R} + \mathbf{r}_2 - \mathbf{r}_1$, is zero in the schematic to elucidate the zero-range Migdal interaction.

interaction, the absence of a pocket structure might be attributed to the inaccuracy of the NN interaction.

Inspired by the nucleus-nucleus potential for fusion and fission reactions [23–25], we attempt to replace the CDM3Y6 interaction with the density-dependent and zero-range Migdal interaction [23–26],

$$v_N(\mathbf{r}_1, \mathbf{r}_2, s) = C_0 \{ F_{in} x(\mathbf{r}_1, \mathbf{r}_2) + F_{ex} [1 - x(\mathbf{r}_1, \mathbf{r}_2)] \} \delta(s). \quad (4)$$

The coordinate system used in the double-folding procedure is shown in Fig. 1. The parameter C_0 denotes the inverse density of states at the Fermi surface, and parameters F_{in} , F_{ex} are the amplitudes of the NN interaction. These parameters are usually determined by fitting the experimental data within the theory of finite Fermi systems [23]. The strength of the interaction between the touching nucleons relates to the density-dependent term $x(\mathbf{r}_1, \mathbf{r}_2)$ which is given by

$$x(\mathbf{r}_1, \mathbf{r}_2) = \frac{\rho_1(\mathbf{r}_1) + \rho_2(\mathbf{r}_2)}{\rho_{00}}. \quad (5)$$

Here, the denominator $\rho_{00} = \frac{\rho_{1,s} + \rho_{2,s}}{2}$ is the mean value of the saturation densities of the interacting nuclei. The term $x(\mathbf{r}_1, \mathbf{r}_2)$, restricted by the δ function, represents the local density overlap between the interacting nuclei. Therefore, the Migdal interaction can effectively describe the variation of NN interaction when the nuclei have different density overlaps. It was evidenced in previous double-folding calculations to describe the nucleus-nucleus potentials for fusions, and in these potentials, a pocket geometry was formed [23–25]. To safely extend the Migdal interaction to α decay, we first neglect the medium effect of the α cluster and analyze the traditional double-folding α -nucleus potential generated with this NN interaction. As an exploratory calculation, the α decay of the typical nucleus ^{212}Po is chosen as an example.

Within the cluster model, the α -nucleus potential V is the sum of the nuclear potential V_N , the Coulomb potential V_C , and the centrifugal term $V_L = \frac{L(L+1)\hbar^2}{2\mu R^2}$ [27]. The traditional double-folding potentials are derived under the frozen-density approximation [19,28]

$$V_{N,C}(\mathbf{R}) = \int \rho_1(\mathbf{r}_1) \rho_2(\mathbf{r}_2) v_{N,C}(s) d\mathbf{r}_1 d\mathbf{r}_2. \quad (6)$$

The density distributions of the daughter nucleus and α cluster are given by $\rho_1(\mathbf{r}_1) = \frac{\rho_{1,s}}{1 + \exp(\frac{r_1 - R_d}{a})}$ and $\rho_2(\mathbf{r}_2) = \rho_{2,s} \exp(-0.7024 r_2^2)$, respectively. The radius R_d and the diffuseness a of the daughter nucleus ^{208}Pb are given by $R_d = 1.07 A_d^{1/3}$ fm and $a = 0.54$ fm. The saturation densities $\rho_{1,s}$ and $\rho_{2,s}$ are determined through the normalization procedures of these density distributions.

With the Coulomb part v_C of the NN interaction being well defined, the nuclear part v_N takes the form of Eq. (4). The interaction parameters are taken as $C_0 = 300$ MeV fm³, $F_{in} = 0.09$, which are well justified by fitting the experimentally measured nuclear properties [23,24]. As for the parameter F_{ex} , it is taken as a variable determined by reproducing the experimental properties with the obtained α -nucleus potential.

To fix F_{ex} , we calculate the α -decay width for the $L = 0$ transition of ^{212}Po using the two-potential approach (TPA) [29]. The TPA allows one to divide the tunneling problem into a bound-state and a scattering problem. The decay width can be expressed with the bound-state wave function $\phi(R)$ and the scattering wave function $\chi_l(kR)$, $\Gamma = \frac{4\hbar^2 \tilde{k}^2}{\mu k} |\phi(\tilde{R}) \chi_l(k\tilde{R})|^2$. Here, $k = \sqrt{2\mu Q_\alpha / \hbar^2}$, $\tilde{k} = \sqrt{2\mu(V(\tilde{R}) - Q_\alpha) / \hbar^2}$, and \tilde{R} is the separation radius chosen as the mean value of the barrier position and the outer classical turning point. While $\phi(R)$ is calculated numerically by solving the Schrödinger equation within the inner potential, $\chi_l(kR)$ can be approximated by the regular Coulomb wave function $F_l(kR)$. Note that the eigenvalue of the bound-state wave function should match the α -decay energy Q_α . In this case, the parameter F_{ex} is determined as -2.53 to reproduce the experimental Q_α .

The derived α -nucleus potential V under the frozen-density approximation is plotted in Fig. 2(a). As expected, the potential has a strong repulsive core and a pocket geometry is naturally formed at the nuclear surface between the repulsive core and the Coulomb barrier. Therefore, it can be inferred that the formation of the pocket structure is closely related to the variation of the NN interaction in the large density-overlap region.

According to the many-body calculation of the QWA, the α -cluster state exists only where the medium density is below the Mott density. This implies that the domain of the α -cluster wave function should be predominantly located in the region beyond the critical radius r_c which denotes the Mott density. As shown in Fig. 2(a), the obtained α -cluster bound-state wave function $\phi(R)$ is located around the center of the pocket. However, the domain of $\phi(R)$ is split by the r_c , with half of it entering the internal region, which contradicts the conclusion from the microscopic calculation. From a physical viewpoint, one can realize that the pocket position shown in Fig. 2(a) is too much inside the core region for the decaying system.

To solve the above problem, a reasonable guess is that the inconsistency of the α -nucleus potential might result from the absence of medium effect in the previous double-folding calculation. As already noted in [10,16,17], the in-medium α cluster exhibits a wider spatial distribution than a free α particle. Compared with the frozen-density approximation, the medium effect influences the overlap of the α -daughter system at different medium densities. Because both the nuclear repulsion and Pauli blocking are sensitive to the density

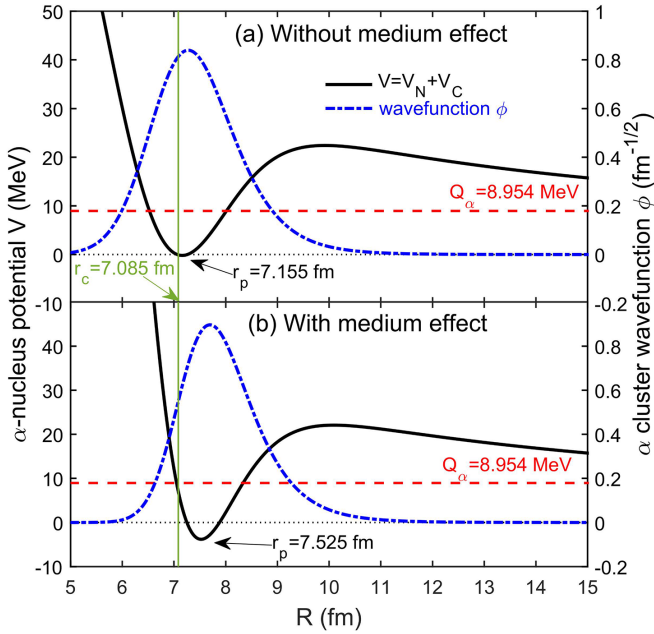


FIG. 2. The α -nucleus potential $V(R)$ and the α -cluster wave function $\phi(R)$ for ^{212}Po : (a) without medium effect, (b) with medium effect. The α decay energy Q_α and the pocket positions r_p are shown. The critical radius r_c , where the medium density is $1/5$ of the saturation density, is marked. Note that after incorporating the medium effect, the pocket and the domain of $\phi(R)$ shift to the surface region specified by r_c . The first classical turning point appears very close to r_c , which nicely matches the physical picture indicated by the microscopic calculation [10].

overlap between the interacting nuclei, a subtle change in the overlap can significantly affect the strength of these interactions, and subsequently, the position of the pocket in the α -nucleus potential.

Therefore, in the next step, we consider the medium effect and calculate the dynamic double-folding potential for ^{212}Po . This potential can be obtained by using Eqs. (1) and (2). Importantly, since the medium effect is embodied in the α -cluster density distribution as illustrated in Eq. (3), corresponding adjustments are also required for the density-dependent term x in the Migdal interaction

$$x(\mathbf{r}_1, \mathbf{r}_2, \mathbf{R}) = \frac{\rho_1(\mathbf{r}_1) + \rho_2(\mathbf{r}_2, \mathbf{R})}{\rho_{00}(\mathbf{R})},$$

$$\rho_{00}(\mathbf{R}) = \frac{\rho_{1,s} + \rho_{2,s}(\mathbf{R})}{2}. \quad (7)$$

Here, we keep the value of C_0 and F_{in} in Eq. (4) unchanged, and F_{ex} is refitted as -3.21 to reproduce the experimental Q_α of ^{212}Po .

Figure 2(b) shows the DDFP generated with the Migdal interaction for ^{212}Po . A comparison between the pocket positions in Figs. 2(a) and 2(b) shows, as expected, that the pocket shifts to a larger R after incorporating the medium effect. As is known, the medium effect embodies the α -cluster dynamics, resulting from the variation of Pauli blocking at different medium densities. It acts on the α cluster as soon as the medium density has a finite value. To consider an inverse

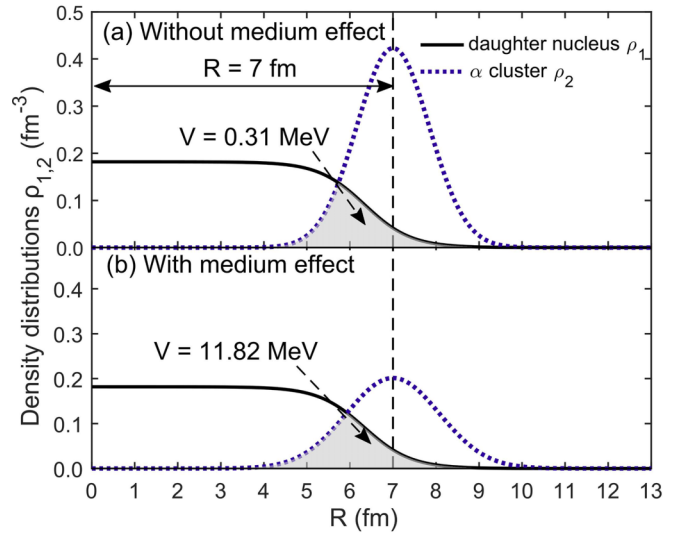


FIG. 3. The density overlap (grey patches) between the daughter nucleus ^{208}Pb and the α cluster at $R = 7$ fm: (a) without medium effect, (b) with medium effect. The center of mass of the α cluster is denoted by the dashed line. The strength of the α -nucleus potential V , determined by the overlaps, is given to illustrate that the repulsion felt by the α cluster is strengthened after incorporating the medium effect.

process of α emission, as the α cluster approaches the core from the tail of the daughter's density distribution, it gradually expands in size and becomes less bound due to the increasing Pauli blocking. Consequently, the α cluster and the daughter nucleus will have larger density overlaps than the case of the frozen-density approximation, as illustrated in Fig. 3. Therefore, the repulsive interaction felt by the α cluster will occur at larger R . This explains how the medium effect influences the position of the repulsive core and the pocket structure.

Apart from the pocket position, another noteworthy finding in Fig. 2(b) is that the first classical turning point appears close to the critical radius. It clearly indicates that once the α cluster crosses the critical radius and enters the classical forbidden region, the strong repulsive core will prevent the α cluster from forming deeply inside the nucleus. As is evidenced in Fig. 2(b), the corresponding α -cluster wave function predominantly disperses beyond the critical radius. This feature nicely matches the physical picture that the α cluster forms at the nuclear surface below a certain nucleon density, which is supported by the microscopic calculation [10].

It is worth noting that the pocket-type potentials were previously studied within the Skyrme energy-density formalism (SEDF) by Seif *et al.* and Denisov *et al.* [21,30–32]. In these studies, the surface pocket appears due to the exchange of intrinsic kinetic energy, as a manifestation of the Pauli repulsion at small interacting distances. For the standard deep potential without a surface pocket, this Pauli repulsion is usually introduced by applying the Wildermuth rule to the quasibound decaying state, which yields a multinode α -cluster wave function. Comparatively, the internal Pauli repulsion is already considered in the pocket-type potential. It leads to a zero-node α -cluster wave function, reflecting the clustering

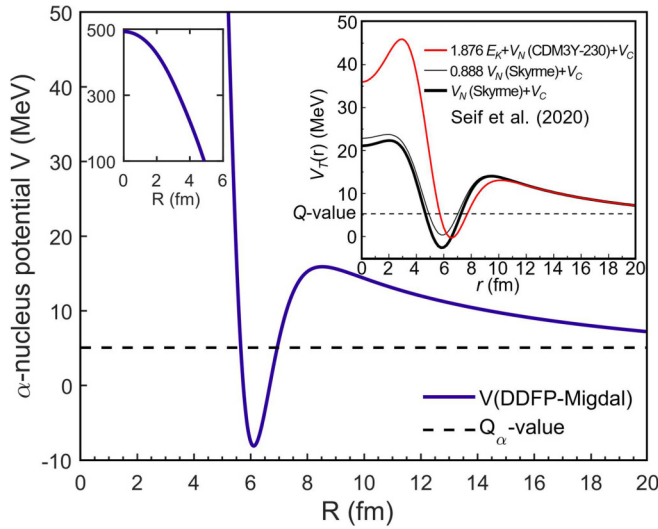


FIG. 4. The α -nucleus potentials V for ^{105}Te in $L = 0$ α transition. The DDFP with Migdal interaction is denoted by the blue solid line. The inset at the left upper corner shows the behavior of the DDFP at $R \rightarrow 0$, while the inset at the right upper corner, taken from Ref. [30] for comparison, shows the potentials constructed with the Skyrme energy-density formalism. The DDFP is similar to that directly derived by the SEDF (black bold line) in terms of the location of the pocket and the height of the Coulomb potential barrier.

feature at the nuclear surface [30]. For comparison, we plot the α -nucleus potential for ^{105}Te with the improved DDFP model in Fig. 4, and the potentials based on the SEDF, taken from [30], are shown in the inset. It turns out that, in terms of the pocket positions (≈ 6.0 fm) and the heights of the Coulomb barrier (≈ 15.0 MeV), the DDFP with Migdal interaction is very similar to that directly derived from the SEDF with Skyrme-SLy4 force. The difference appears in the core region where the repulsive interaction of the DDFP-Migdal potential is much stronger. Despite the pocket generated in different methods, a common physics is shared: the strong Pauli repulsion emerging from the large density-overlap regions is responsible for the formation of the pocket.

Based on the exploratory calculations above, the physics of the formed pocket structure in the α -nucleus potential becomes transparent. In the next step, we extend the calculation to the favored α decays of the nearby even-even Pb, Po, and Rn isotopes, as a further verification for the present model. With F_{ex} already determined in the case of ^{212}Po , we keep the interaction parameters unchanged in the following calculations and adjust the diffuseness parameter a of the daughter nucleus to reproduce the experimental Q_α . Interestingly, we find the diffuseness determined in the reproduction shows a clear negative linear correlation with the Q_α value of its corresponding parent nucleus, as demonstrated in Fig. 5. Besides, the $N_d = 126$ shell effect is well reproduced in the variation of a . These features are easy to understand. Because along the same isotopic chain, when the daughter nucleus is closer to a shell closure, it becomes more tightly bound and exhibits a smaller diffuseness. On the other hand, the Q_α of its parent nucleus is relatively higher than the neighboring α emitters.

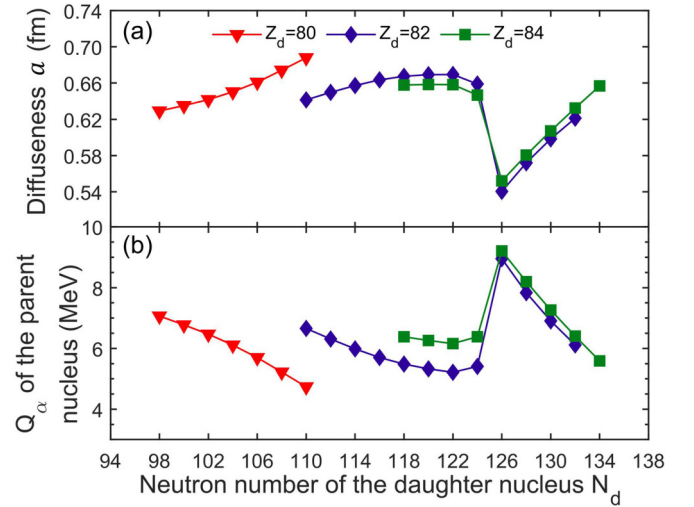


FIG. 5. (a) The determined surface diffuseness of the daughter nucleus as a function of its neutron number. (b) The experimental α decay energy of the parent nucleus as a function of its daughter's neutron number. The variation of diffuseness appears as a reverse pattern of the Q_α , showing an evident shell effect at $N_d = 126$.

Apart from the above finding, it is well known that the shell effect also exists in the systematics of α -preformation factors for nuclei in this region [1, 16, 33, 34]. In Fig. 6, α -preformation factors, calculated using $P_\alpha = \Gamma^{\text{exp}}/\Gamma$, are shown as a function of the neutron number of parent nucleus. For comparison, we also show the P_α recalculated in the TPA with the prior DDFP-CDM3Y6 model [16]. As shown in Fig. 6, the $N_p = 126$ shell effect is reproduced by both models and the P_α variation for each isotopic chain is basically similar. Notable differences can be found in the magnitude of these P_α factors, in which the results at $N_p \leq 126$ from the DDFP-Migdal model are generally smaller in one order of magnitude.

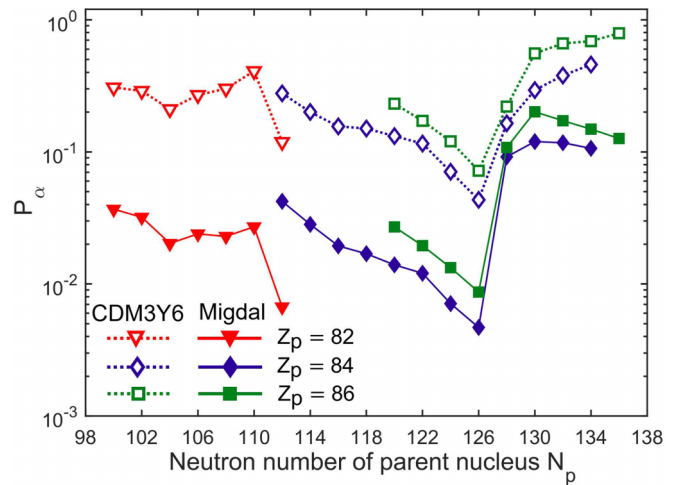


FIG. 6. The extracted α -preformation factor P_α for even-even Pb, Po, and Rn isotopes. The DDFP generated with Migdal (solid lines) and CDM3Y6 (dotted lines) NN interactions yield a similar trend for the P_α variation, in which the well-known neutron $N_p = 126$ shell effect and the proton $Z_p = 82$ shell effect are both reproduced.

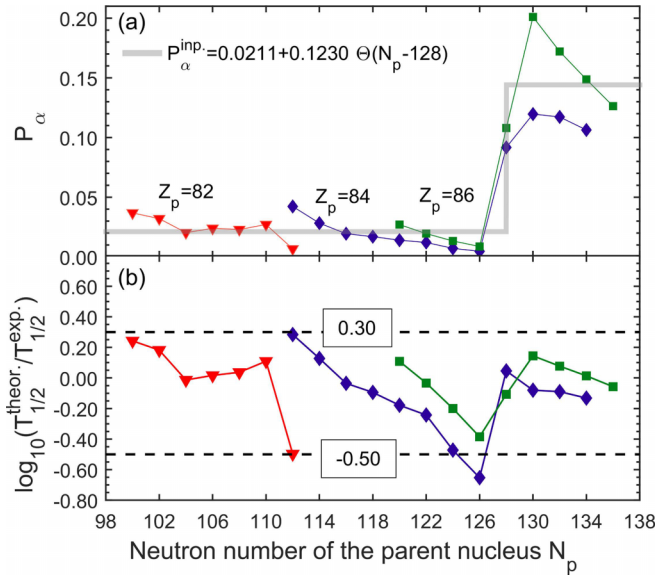


FIG. 7. (a) The input α -preformation factor P_α^{inp} . (grey bold line) in the half-life calculation and the extracted P_α (colored symbols) are shown for comparison. (b) The logarithmic deviation between the theoretical and experimental α decay half-lives. The range of the deviations indicates a factor of 2–3 between the theoretical and experimental values.

Besides, the P_α variations at $N_p > 130$ also seem different for the two models. The DDFP-Migdal model shows a more rapid saturation in the preformation probability beyond $N_p = 130$. All these differences demonstrate the model dependence of the present calculations in which the P_α factors are extracted from the experimental decay widths. The magnitude and the variation of P_α should be verified through future microscopic calculations.

After the P_α systematics is verified, we examine the applicability of the DDFP-Migdal model to half-life calculations. The theoretical α -decay half-life is calculated by $T_{1/2}^{\text{theor.}} = \frac{\hbar \ln 2}{P_\alpha F}$. The input P_α factor can be reasonably approximated by a simple expression $P_\alpha^{\text{inp}}(N_p) = P_0 + P_1 \Theta(N_p - 128)$, where $\Theta(x)$ is the Heaviside step function with $\Theta(0) = 0.5$. The parameters $P_0 = 0.0211$, $P_1 = 0.1230$ are determined by fitting the expression to the extracted P_α from experimental decay widths, as illustrated in Fig. 7(a).

Figure 7(b) shows the deviations between the theoretical and experimental half-lives. The logarithmic deviations are mostly within -0.5 – 0.3 , indicating a factor of 2–3. A statistical analysis shows an average deviation $\sigma = 0.1689$, with the definition $\sigma = \frac{1}{N} \sum_{i=1}^N |\log_{10} T_{1/2,i}^{\text{theor.}} - \log_{10} T_{1/2,i}^{\text{exp.}}|$. Large deviations mainly occur at $N_p = 126$ and $N_p = 112$. The for-

mer corresponds to the well-known neutron shell effect, while the latter is due to the proton shell effect at $Z_p = 82$, which results in a significant increase in the P_α from $Z_p = 82$ to 84. Note that we adopt the constant $P_\alpha^{\text{inp}} = 0.0211$ for nuclei with $N_p \leq 126$ to calculate their half-lives. The evident difference between the results of ^{194}Pb and ^{196}Po is attributed to the large deviation between P_α^{inp} and the extracted P_α at $N_p = 112$. In general, the experimental α -decay half-lives are fairly well reproduced with the improved DDFP. It is expected that the present model still can be refined with pertinent considerations on nuclear deformation and diffuseness anisotropy [17,35,36], which might further improve its accuracy.

In summary, in this Letter, we explore the underlying physics in the formation of a pocket structure in the α -nucleus potential based on the DDFP model. We improve the NN interaction in the DDFP and combine it with the medium effect. The final potential successfully generates a pocket in the surface region where the nucleon density is below the Mott density. The pocket’s formation is attributed to the strong Pauli repulsion inside the core region, which requires the NN interaction to have proper density dependence in the large density-overlap region. The medium effect is essential to the position of the formed pocket structure. The resulting α -cluster wave function exhibits a peak at the pocket center, reproducing the α -clustering feature indicated in the microscopic calculations. Besides, the improved DDFP is validated by calculating the diffuseness, α -preformation factors, and α -decay half-lives. The good reproduction of the shell effects and experimental half-lives confirms the reliability of the improved potential. The result of this study brings a new insight into the clustering phenomenon in heavy nuclei, which might be helpful for the understanding of the microscopic mechanism of α decay.

To go beyond the present study, it would be meaningful to explore the applicability of the pocket-type DDFP in the description of other properties, such as rotational bands, $B(E2)$ transition strengths, and fusion cross sections. These properties were widely studied by using the standard deep potentials without a surface pocket [37–40]. A comparative analysis between the two types of potentials might help us further the understanding of the structural effects and the interactions in different nuclear processes.

This work is supported by the National Natural Science Foundation of China (Grants No. 12035011, No. 11975167, No. 12175151, No. 12005139, and No. 11947123), the Guangdong Major Project of Basic and Applied Basic Research (Grant No. 2021B0301030006), the Steady Support Program for Higher Education Institutions of Shenzhen (Grants No. 20200810163629001 and No. 20200817005440001).

[1] R. Bonetti and L. Milazzo-Colli, *Phys. Lett. B* **49**, 17 (1974).
 [2] Z. Ren and G. Xu, *Phys. Rev. C* **36**, 456 (1987).
 [3] G. Royer and R. Gherghescu, *Nucl. Phys. A* **699**, 479 (2002).

[4] S. N. Liddick, R. Grzywacz, C. Mazzocchi, R. D. Page, K. P. Rykaczewski, J. C. Batchelder, C. R. Bingham, I. G. Darby, G. Drafta, C. Goodin, C. J. Gross, J. H. Hamilton, A. A. Hecht, J. K. Hwang, S. Ilyushkin, D. T. Joss, A. Korgul,

- W. Królás, K. Lagergren, K. Li *et al.*, *Phys. Rev. Lett.* **97**, 082501 (2006).
- [5] P. Mohr, *Phys. Rev. C* **73**, 031301(R) (2006).
- [6] K. Auranen, D. Seweryniak, M. Albers, A. D. Ayangeakaa, S. Bottoni, M. P. Carpenter, C. J. Chiara, P. Copp, H. M. David, D. T. Doherty, J. Harker, C. R. Hoffman, R. V. F. Janssens, T. L. Khoo, S. A. Kuvín, T. Lauritsen, G. Lotay, A. M. Rogers, J. Sethi, C. Scholey *et al.*, *Phys. Rev. Lett.* **121**, 182501 (2018).
- [7] H. Takemoto, M. Fukushima, S. Chiba, H. Horiuchi, Y. Akaishi, and A. Tohsaki, *Phys. Rev. C* **69**, 035802 (2004).
- [8] D. Brink and J. Castro, *Nucl. Phys. A* **216**, 109 (1973).
- [9] G. Röpke, A. Schnell, P. Schuck, and P. Nozières, *Phys. Rev. Lett.* **80**, 3177 (1998).
- [10] G. Röpke, P. Schuck, Y. Funaki, H. Horiuchi, Z. Ren, A. Tohsaki, C. Xu, T. Yamada, and B. Zhou, *Phys. Rev. C* **90**, 034304 (2014).
- [11] K. Varga, R. G. Lovas, and R. J. Liotta, *Phys. Rev. Lett.* **69**, 37 (1992).
- [12] M. Patial, R. J. Liotta, and R. Wyss, *Phys. Rev. C* **93**, 054326 (2016).
- [13] C. Xu, Z. Ren, G. Röpke, P. Schuck, Y. Funaki, H. Horiuchi, A. Tohsaki, T. Yamada, and B. Zhou, *Phys. Rev. C* **93**, 011306(R) (2016).
- [14] S. Yang, C. Xu, G. Röpke, P. Schuck, Z. Ren, Y. Funaki, H. Horiuchi, A. Tohsaki, T. Yamada, and B. Zhou, *Phys. Rev. C* **101**, 024316 (2020).
- [15] S. Yang, C. Xu, and G. Röpke, *Phys. Rev. C* **104**, 034302 (2021).
- [16] D. Deng and Z. Ren, *Phys. Rev. C* **96**, 064306 (2017).
- [17] D. Deng, Z. Ren, and N. Wang, *Phys. Lett. B* **795**, 554 (2019).
- [18] D. T. Khoa, G. R. Satchler, and W. von Oertzen, *Phys. Rev. C* **56**, 954 (1997).
- [19] G. R. Satchler and W. G. Love, *Phys. Rep.* **55**, 183 (1979).
- [20] D. S. Delion, S. Peltonen, and J. Suhonen, *Phys. Rev. C* **73**, 014315 (2006).
- [21] W. M. Seif, A. M. H. Abdelhady, and A. Adel, *J. Phys. G: Nucl. Part. Phys.* **45**, 115101 (2018).
- [22] V. Y. Denisov and N. A. Pilipenko, *Phys. At. Nucl.* **73**, 1152 (2010).
- [23] G. G. Adamian, N. V. Antonenko, R. V. Jolos, S. P. Ivanova, and O. I. Melnikova, *Int. J. Mod. Phys. E* **05**, 191 (1996).
- [24] G. G. Adamian, N. V. Antonenko, H. Lenske, S. V. Tolokonnikov, and E. E. Saperstein, *Phys. Rev. C* **94**, 054309 (2016).
- [25] N. V. Antonenko, G. G. Adamian, V. V. Sargsyan, and H. Lenske, *Eur. Phys. J. A* **58**, 211 (2022).
- [26] A. B. Migdal, *Sov. Phys. Usp.* **10**, 285 (1967).
- [27] B. Buck, A. C. Merchant, and S. M. Perez, *Phys. Rev. Lett.* **72**, 1326 (1994).
- [28] C. Xu and Z. Ren, *Nucl. Phys. A* **760**, 303 (2005).
- [29] S. A. Gurvitz and G. Kalbermann, *Phys. Rev. Lett.* **59**, 262 (1987).
- [30] W. M. Seif, A. M. H. Abdelhady, and A. Adel, *Phys. Rev. C* **101**, 064305 (2020).
- [31] W. M. Seif, M. M. Botros, and A. I. Refaie, *Phys. Rev. C* **92**, 044302 (2015).
- [32] O. Davydovska, V. Denisov, and V. Nesterov, *Nucl. Phys. A* **989**, 214 (2019).
- [33] Y. Qian and Z. Ren, *Sci. China Phys. Mech. Astron.* **56**, 1520 (2013).
- [34] Z. Y. Zhang, H. B. Yang, M. H. Huang, Z. G. Gan, C. X. Yuan, C. Qi, A. N. Andreyev, M. L. Liu, L. Ma, M. M. Zhang, Y. L. Tian, Y. S. Wang, J. G. Wang, C. L. Yang, G. S. Li, Y. H. Qiang, W. Q. Yang, R. F. Chen, H. B. Zhang, Z. W. Lu *et al.*, *Phys. Rev. Lett.* **126**, 152502 (2021).
- [35] Z. Wang and Z. Ren, *Phys. Rev. C* **106**, 024311 (2022).
- [36] Z. Wang, D. Bai, and Z. Ren, *Phys. Rev. C* **105**, 024327 (2022).
- [37] F. Hoyler, P. Mohr, and G. Staudt, *Phys. Rev. C* **50**, 2631 (1994).
- [38] Y. Qian and Z. Ren, *J. Phys. G: Nucl. Part. Phys.* **43**, 065102 (2016).
- [39] R. Kumar, S. Rana, M. Bhuyan, and P. Mohr, *Phys. Rev. C* **105**, 044606 (2022).
- [40] M. A. Souza and H. Miyake, *Eur. Phys. J. A* **59**, 74 (2023).